Kinetically Induced Memory Effect in Li-ion Batteries

Supplementary information

Pierfrancesco Ombrini[1,†], Qidi Wang[1,†], Alexandros Vasileiadis[1], Fangting Wu[2], Ziyao Gao[2], Xia Hu[2], Martijn van Hulzen[1], Baohua Li[2], Chenglong Zhao[1,*], Marnix Wagemaker[1,*]

[1]Department of Radiation Science and Technology, Delft University of Technology, Delft, 2629JB, the Netherlands.
[2]Shenzhen Key Laboratory on Power Battery Safety and Shenzhen Geim Graphene Center, School of Shenzhen International Graduate School, Tsinghua University, Guangdong, 518055, China.
[†]P.O. and Q.W. contributed equally to this work.
*Corresponding author. Email: c.zhao-1@tudelft.nl; m.wagemaker@tudelft.nl.

1. Supplementary Results

a. Electrochemical experiments

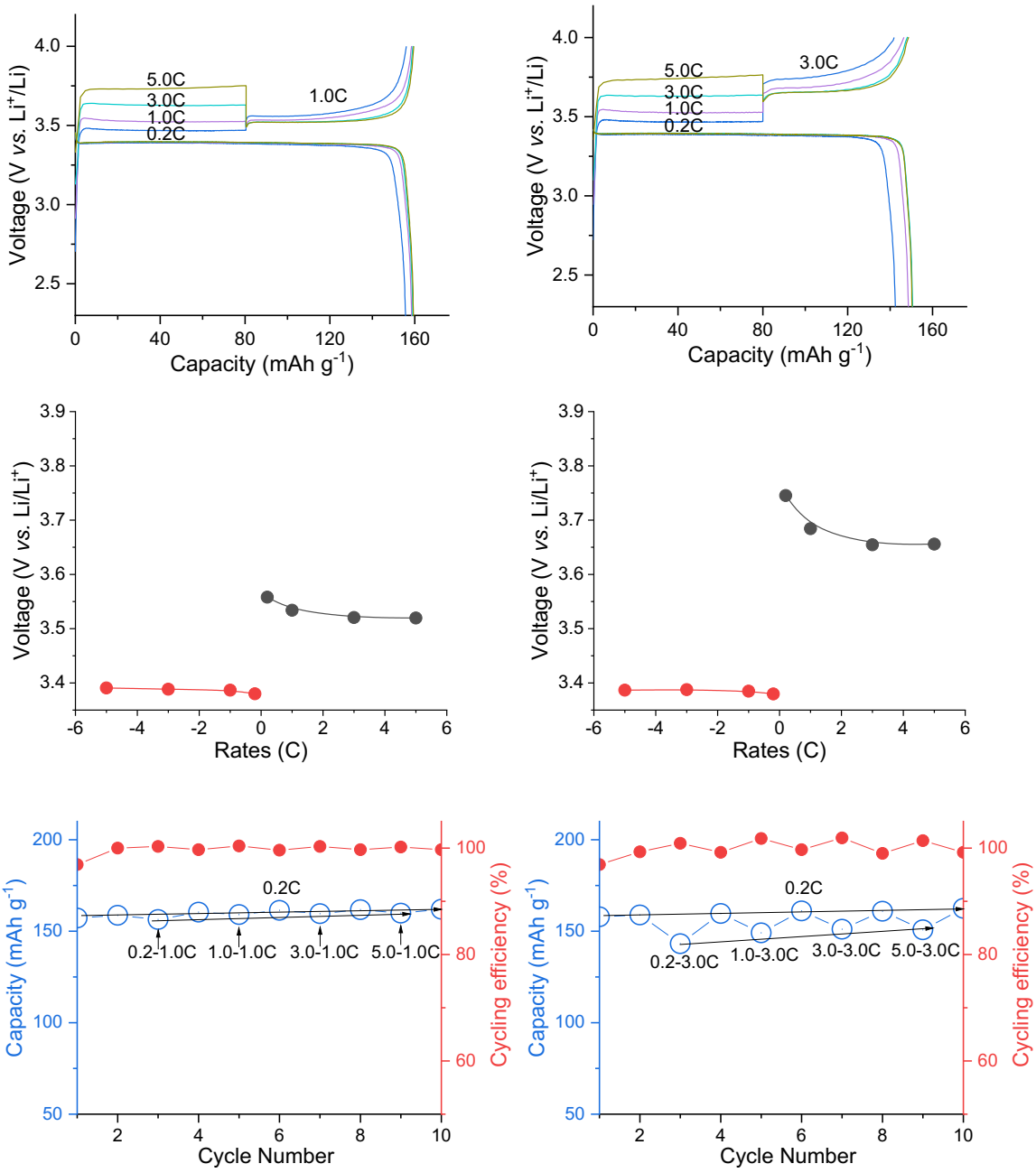

Supplementary information Fig. S1. Voltage vs capacity evolution of an LFP||Li cell during the memory protocol. The voltage profile for LFP at 1.0C in the reading step (left column), and 3.0C in the reading step (right column), respectively (1.0C=150 mA g^{-1}). The overpotential tends to decrease with an increased charging rate in the writing step (center figures), while the capacity tends to increase. The difference between the plateau potentials is reduced if the reading step is executed at a lower rate (lower figure).

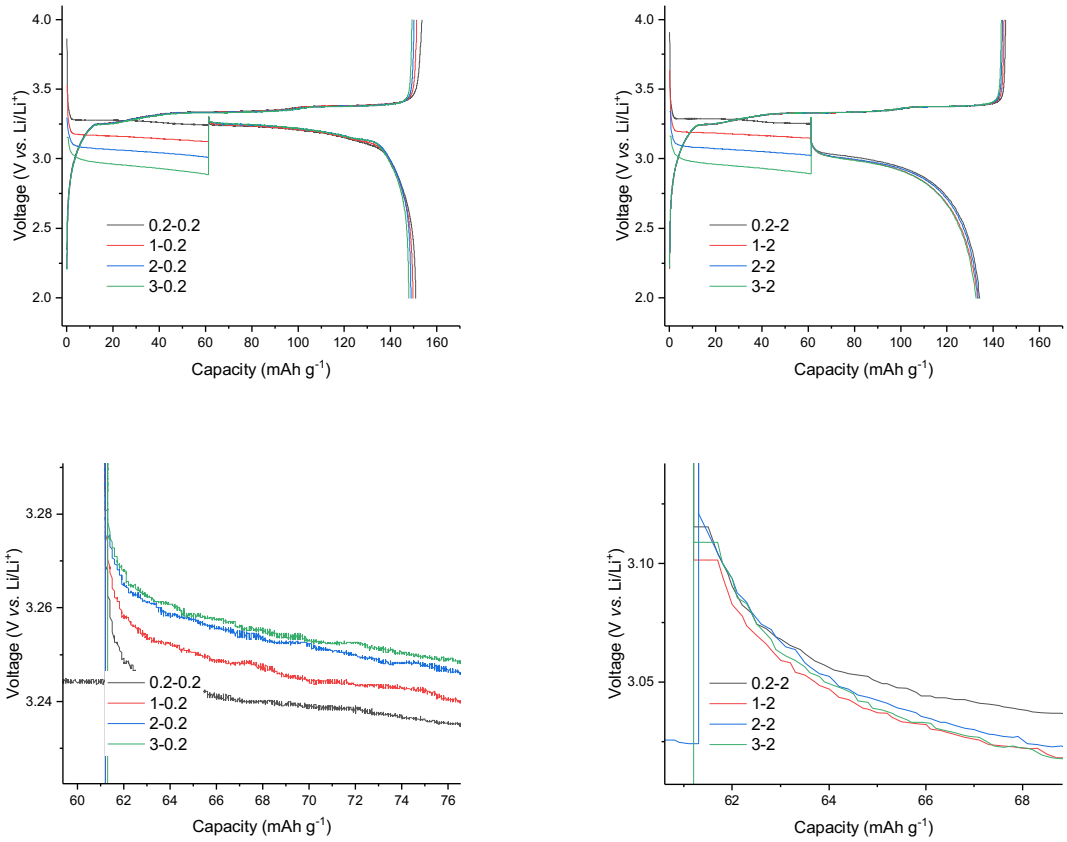

Supplementary information Fig. S2. Voltage vs capacity evolution of an LFP||Graphite cell during a discharge memory protocol. The voltage profile of LFP||Graphite at 0.2C in the reading step (left column), and 2.0C in the reading step (right column), respectively (1.0C=150 mA g^{-1}). Corresponding enlarged figures of initial overpotentials (lower figures).

The memory protocol applied to an LFP||Graphite full cell during discharge shows the presence of the kinetically induced memory effect. In particular, if the reading step is performed at low rates (0.2C) a reduced overpotential is visible, while performing a 2.0C reading step do not show a specific trend. The origin of this discrepancy can be found in the counteracting effect of LFP and Graphite heterogeneities. Low reading rates can show the reduced reaction overpotential, originating from the higher LFP active particle population (Fig. S21). The overpotential of higher rates is instead dependent on multiple factors, such as uneven Li distribution in the graphite particles. This hinder the LFP's memory effect and do not allow the full cell voltage to significantly change. A full cell's behavior is so dependent on the kinetic limitations of both electrodes, and it is therefore not possible to generalize the phenomenon. The experiment was performed during discharge to allow for high rates, since high charging rates might initiate Li plating on graphite particles and significantly change the electrode's properties.

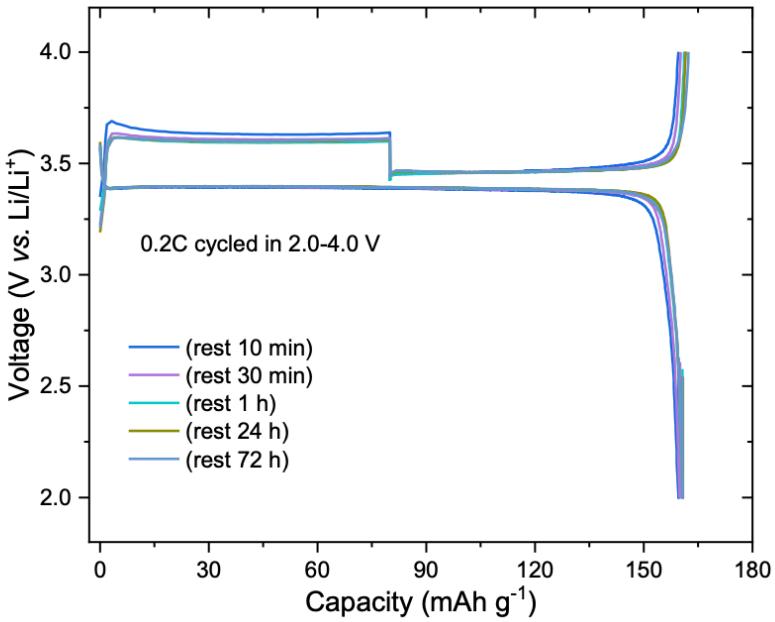

Supplementary information Fig. S3. Voltage vs capacity evolution of LFP||Li cells during the memory protocol cycle at different resting times. The charging rate is 3.0C during the writing step and 0.2C during the reading step. No relevant differences can be found at different resting times indicating that the long-lasting effect of particle-level heterogeneities created during the writing step.

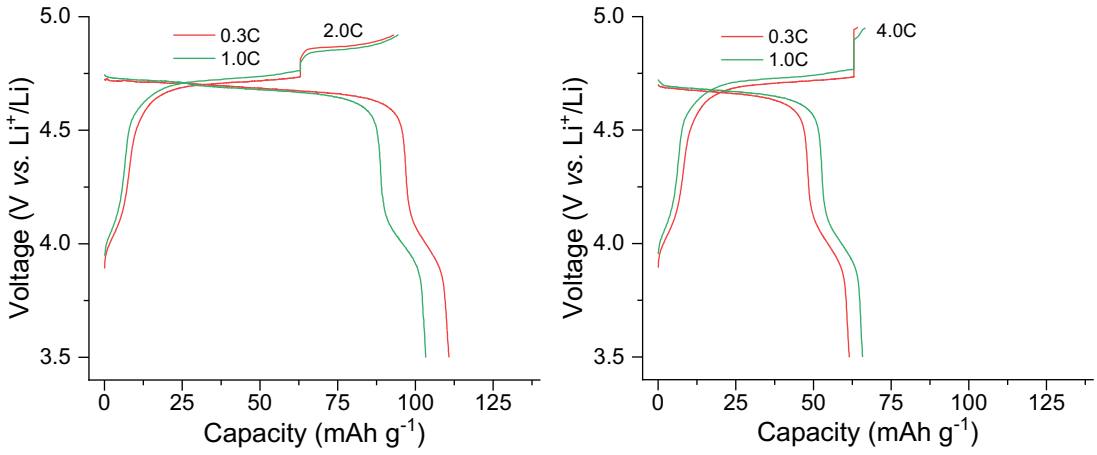

Supplementary information Fig. S4. Voltage profile of $LiNi_{0.5}Mn_{1.5}O_4$||Li cells during the memory protocol. The charging rate is 0.3C/1.0C in the writing step, 0.2C/2.0C/4.0C in the reading step, and 0.1C in the discharge (1.0C=147 mA g^{-1}). The kinetically induced memory effect is also present in LiNi0.5Mn1.5O4, being a phase-separating material, but due to the smaller miscibility gap it is less pronounced.

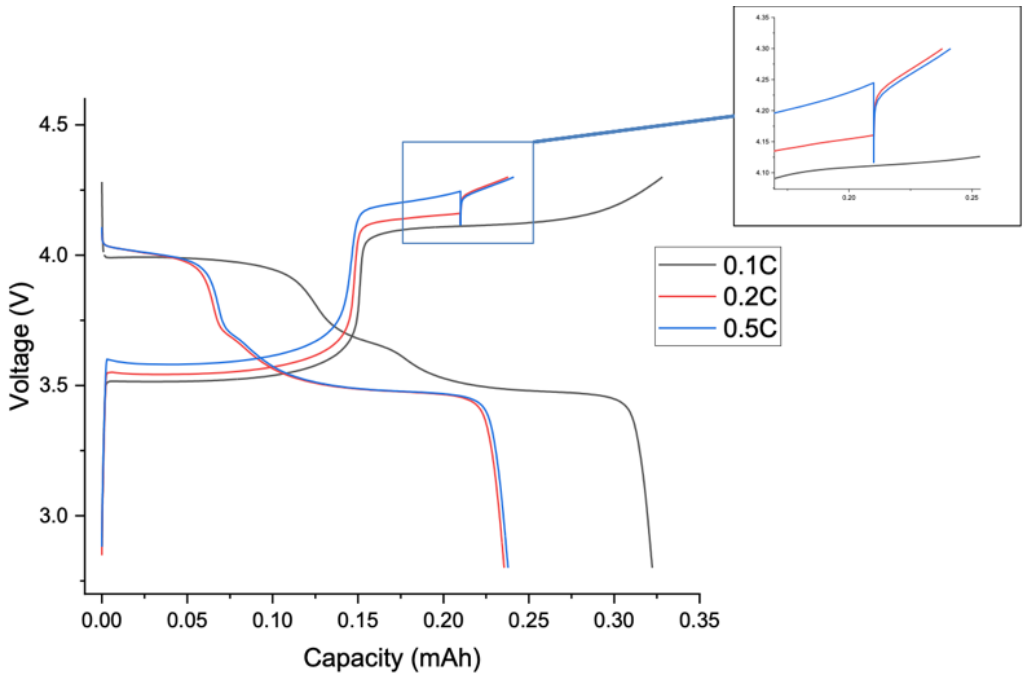

Supplementary information Fig. S5. Voltage profile of $LiMn_{0.4}Fe_{0.6}PO_4$||Li cells during the memory protocol. The charging rates are 0.2C and 0.5C in the writing step, and 0.3C in the reading step (1.0C=150 mA g^{-1}). The kinetically induced memory effect is also present in $LiMn_{0.4}Fe_{0.6}PO_4$, in particular, the Mn plateau of this composition is phase-separating[1] with a reduced miscibility gap.

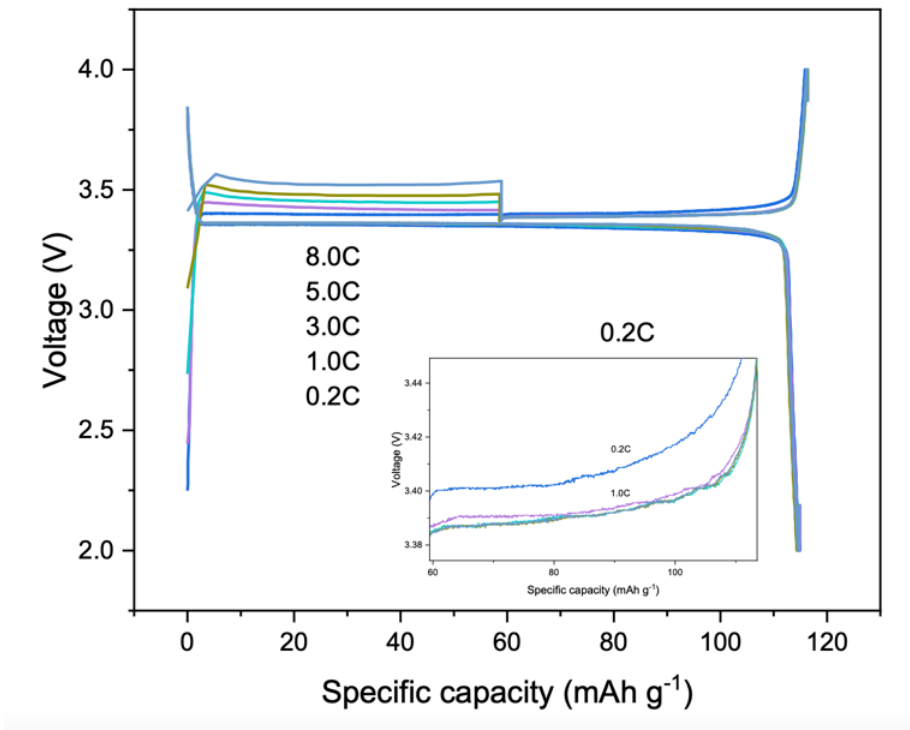

Supplementary information Fig. S6. Voltage profile of $Na_3V_2(PO_4)_3$||Na cells during the memory protocol. The charging rates are 0.2C/8.0C in the writing step, and 0.2C in the reading step (1.0C=110 mA g^{-1}). The kinetically induced memory effect is shown to be general to every phase separating insertion compound for rechargeable batteries beyond the Li-ion batteries.

b. Material characterization

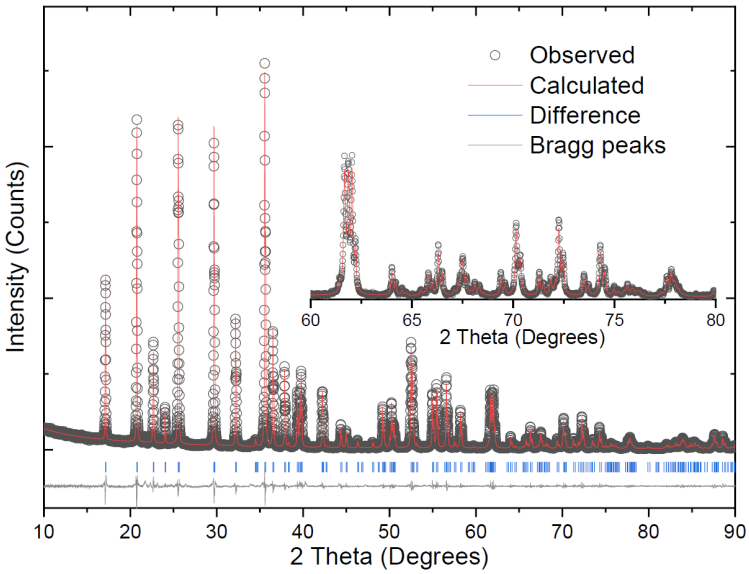

Supplementary information Fig. S7. The XRD Rietveld refinement of $LiFePO_4$ material used in this study. The patterns of the sample show the formation of orthorhombic $LiFePO_4$ crystal structure (space group: Pnma), commonly known as olivine type phase.

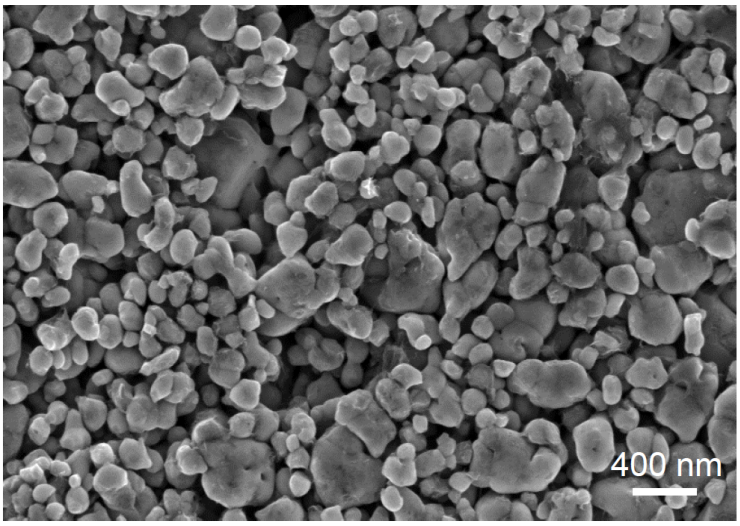

Supplementary information Fig. S8. SEM image of $LiFePO_4$ material used in this study. According to the SEM images of the $LiFePO_4$ material, the particle size is in the range of 100-500 nm.

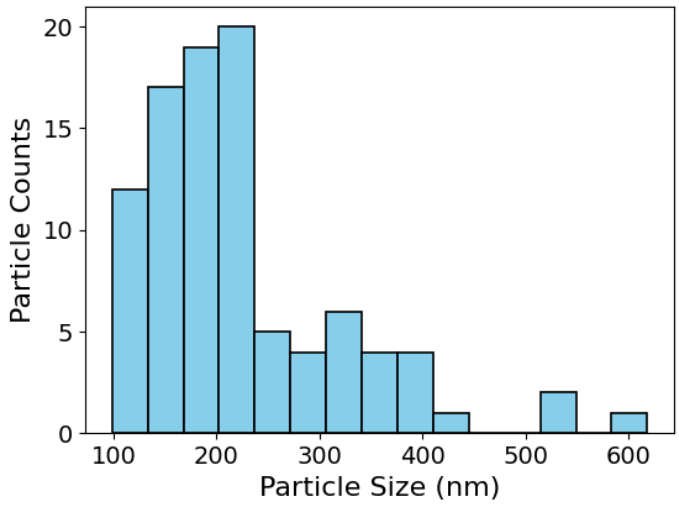

Supplementary information Fig. S9. Particle size distribution $LiFePO_4$ material used in this study. According to the SEM images of the $LiFePO_4$ material, the particle size distribution is a lognormal distribution with an average of 200 nm.

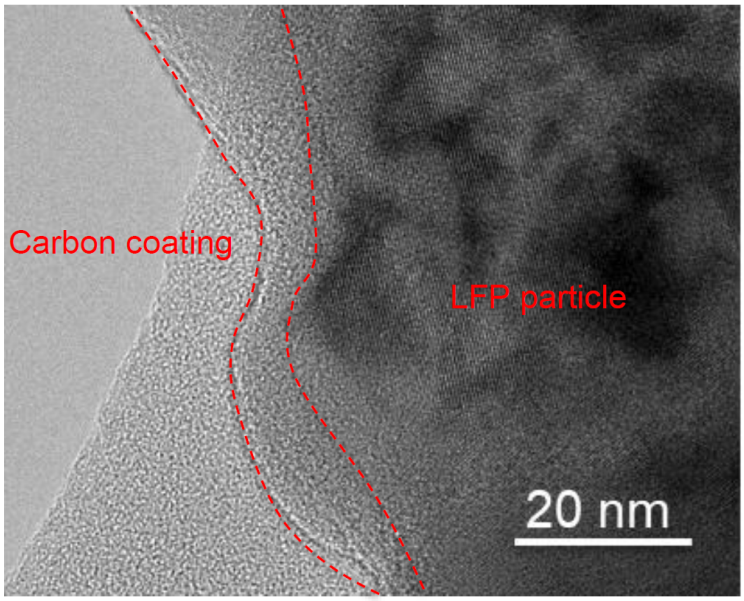

Supplementary information Fig. S10. TEM image of $LiFePO_4$ material used in this study. The $LiFePO_4$ particle is coated with an amorphous carbon layer with a thickness around 10 nm.

c. Electrochemical phase-field modeling

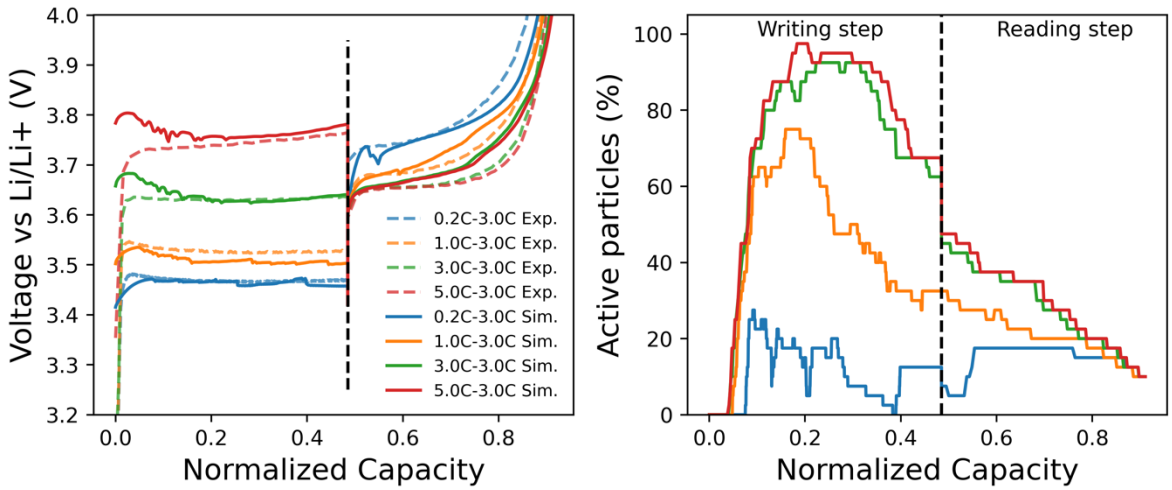

Supplementary information Fig. S11. Comparison between the experimental and the simulated voltage curves for the memory cycles on $LiFePO_4$ (left) and evolution of the active particle population during the application of the memory cycles on $LiFePO_4$ (right).

The electrochemical phase-field simulation can reproduce the kinetically induced memory effect and the capacity loss for the LFP case. The model can so be considered the first one capable of fitting the voltage curves of a complex protocol by incorporating the phase separation mechanism and the relevant sources of overpotential with a purely physics-based approach. The resulting active particle population dynamics also shows how the increased active particles at the beginning of the readings step is responsible for the lower overpotential.

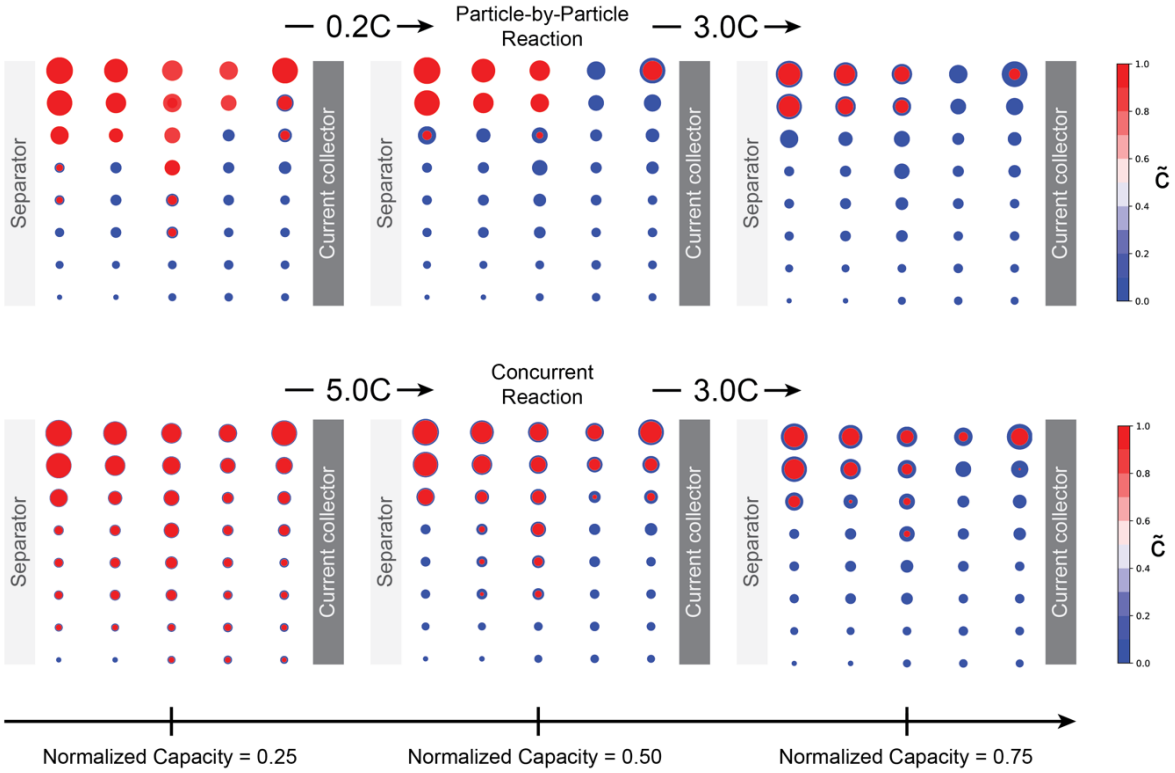

Supplementary information Fig. S12. Evolution of the concentration inside the simulated particles during the 0.2C-3.0C (upper) and 5.0C-3.0C (lower) memory protocols. 0.2C and 5.0C rates refer to the writing rates, the reading rate was set to 3.0C.

The simulations can also show the evolution of the concentration inside each particle. We can observe the particle-by-particle reaction taking place at 0.2C leading to a mosaic state at 50%SOC, while the 5.0C case proceeds by utilizing most of the available particles. The phase-field simulation is capable of obtaining a shrinking core mechanism without the imposition of any sudden phase change leading to a realistic result.

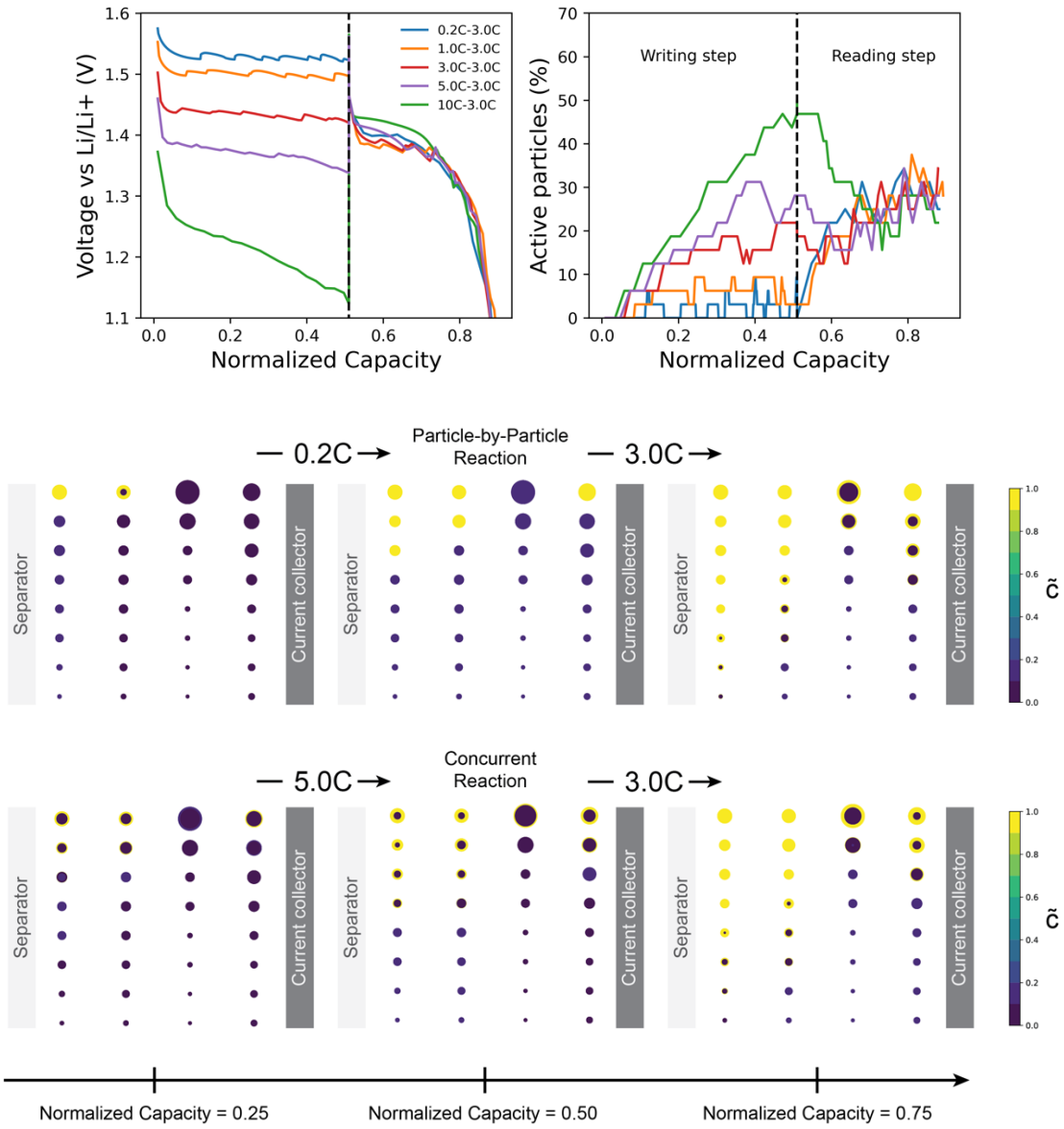

Supplementary information Fig. S13. Simulation of the kinetically induced memory effect on $Li_4Ti_5O_{12}$. Voltage responses during to the memory protocols (upper left), active particle population dynamics (upper right), evolution of the solid concentration during the 0.2C-3.0C and 5.0C-3.0C memory protocols (bottom).

The model developed by Vasileiadis et al.[2] was adapted by considering wiring effects and used to investigate the effect of the memory protocol the lithiation of $Li_4Ti_5O_{12}$. The numerical results, in line with the experiments, prove the presence of this effect being general for phase-separating materials, and being regulated by the same phenomena. The active particle population is following the same trend observed in the LFP case. The absence of a saturation current is explained by the higher exchange current density of $Li_4Ti_5O_{12}$ which limits the active particle population. The simulations are capable of showing the mosaic lithiation for the case of 0.2C writing step in comparison to the collective intercalation for the 5.0C case.

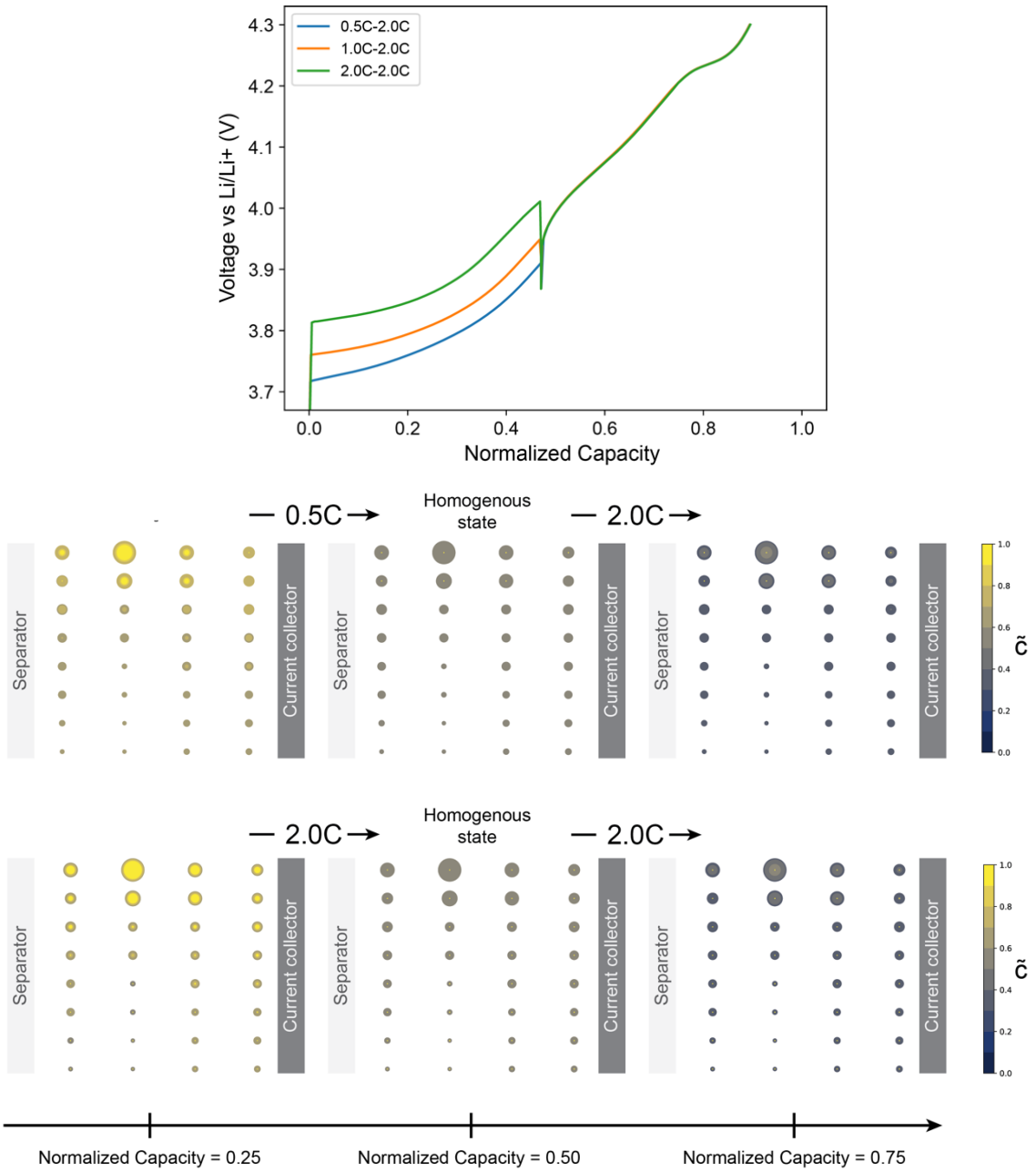

Supplementary information Fig. S14. Simulation of the effects of the memory protocol on $LiNi_{0.8}Mn_{0.1}Co_{0.1}O_2$. Voltage responses during to the memory protocols (upper), evolution of the solid concentration during the 0.2C-3.0C and 5.0C-3.0C memory protocols (bottom).

By implying a validated model of NMC811[3] to simulate the electrochemical behavior under the effect of the memory protocol, we observe how the different rates hardly influence the collective dynamics in a diffusion-limited solid-solution system. After the relaxation, the particles equilibrate internally and exchange lithium with each other, resulting in the same state despite the writing rate. This naturally leads to the same voltage response to the subsequent applied current.

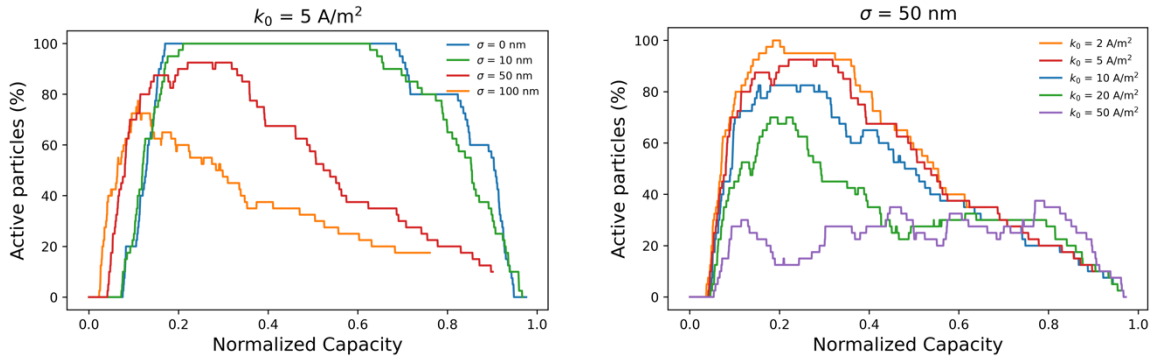

Supplementary information Fig. S15. Active particle population dynamics of the LFP electrode, for various standard deviation of the particle size distribution σ (left) and exchange current densities k_0 (right), during a 3.0C constant current charge.

Our findings indicate that variations in the standard deviation of the particle size distribution (σ) significantly affect the symmetry of the active particle population evolution. Smaller particles tend to initiate the phase transition earlier, and because they also complete the delithiation process before larger particles, the system struggles to sustain a high active particle fraction throughout the reaction. In contrast, a narrower particle size distribution promotes a more synchronized reaction across particles, as they exhibit similar nucleation barriers and kinetic properties. As a result, the active particle population remains more stable during the charging process. The exchange current density (k_0), on the other hand, primarily acts as a scaling factor that governs the balance between the overall electrode reaction time and the reaction time of individual particles[4]. Higher k_0 values enable the system to sustain the current by activating fewer particles at the same rate, effectively reducing the required active particle fraction. This behavior is illustrated in Fig. S15, which shows how increased k_0 shifts the burden of charge transfer onto fewer particles while maintaining the same applied current. Ultimately, while the evolution of the active particle population is strongly influenced by the particle size distribution, the maximum active population at a given rate scales proportionally with the charge transfer resistance. These findings highlight the intricate interplay between particle-level kinetics and macroscopic electrochemical response, reinforcing the importance of considering both parameters when modeling and optimizing phase-separating battery materials.

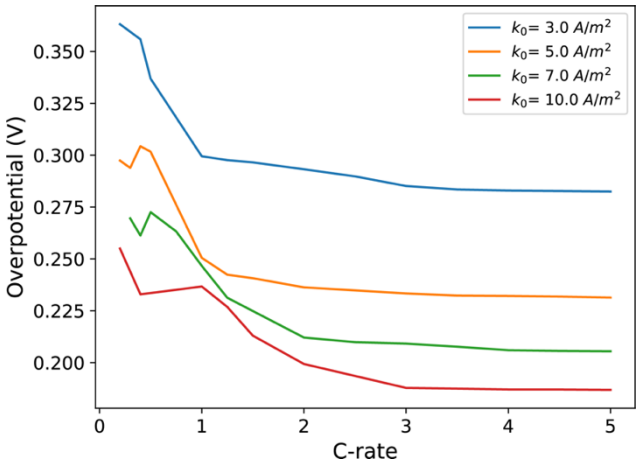

Supplementary information Fig. S16. Effect of LFP exchange current density (k_0) on the initial overpotential of the reading step. The x-axis refers to the writing rate, the reading rate was set to 3.0C.

By changing the exchange current density and applying the memory cycle on the same model utilized previously we observe how the saturation current is strongly dependent on this parameter. We can in fact observe how increasing this parameter, not only the overpotential is reduced, but also the saturation current is driven towards higher rates. While the change in overpotential can be unidentifiable since it is possible to compensate for it by changing other limiting factors such as electrical conductivity or tortuosity, the saturation current is instead strongly related to k_0. This underlines the use of this protocol for the parameter estimation of this usually unidentifiable parameter[5].

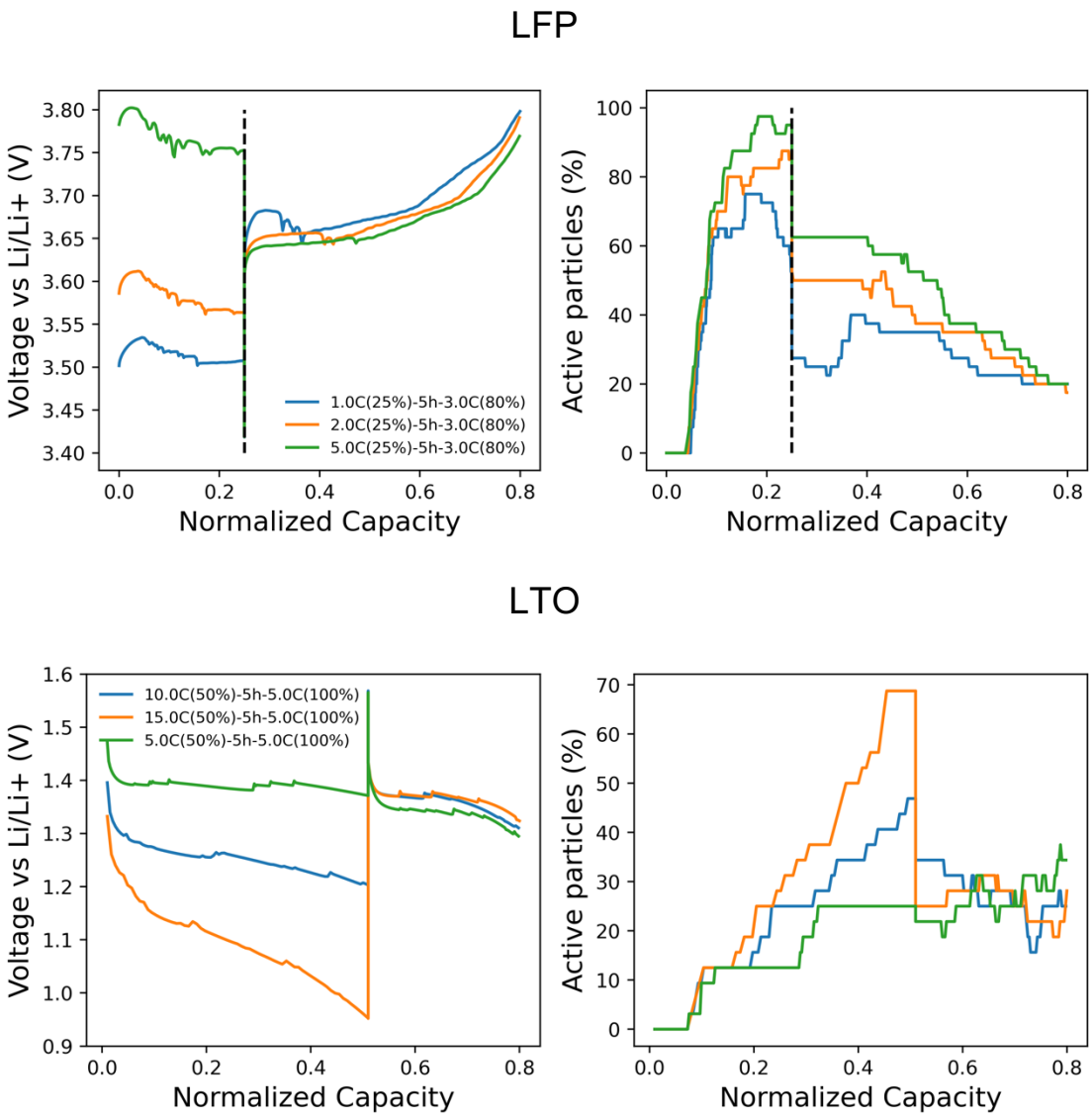

Supplementary information Fig. S17. Examples of voltage and active particle populations during optimize protocols for LFP (upper figure) and LTO (lower figure) electrodes.

Optimized protocols for battery charging, have the multi-objective goals, such as minimizing the energy expenditure and ensuring correct heat management. To explore the implications of the kinetically induced memory effect in practical battery operation scenarios, we employed our validated electrochemical model to simulate realistic charging strategies for LFP and LTO electrodes, focusing on coupling battery operation with electricity pricing. Specifically, we examined scenarios where batteries are integrated within energy storage systems, and charging schedules are strategically aligned with variable electricity prices.

We considered the following scenario: a battery initially at 0% SOC is first partially charged and subsequently brought to 80% SOC, five hours later. Such a scenario commonly occurs in practice, as batteries cannot remain fully discharged for prolonged periods without experiencing degradation.

Consequently, the operator of the energy storage system must perform an initial partial charge step to protect battery longevity, followed by a later charging step that can be strategically aligned with favorable electricity prices or grid conditions. While it is intuitive that the reached SOC and charging rate influence the energy expended during the initial charging, our findings highlight that—due to the kinetically induced memory effect—these initial parameters also significantly influence the overpotential observed during the subsequent charging step, five hours later.

For the LFP electrode, we observe that the active particle fraction peaks at approximately 25% SOC (Fig. 3). Therefore, it can be advantageous to initially charge the battery to around 25% SOC, maximizing particle activation. However, the initial charging rate significantly influences subsequent charging efficiency due to the memory effect. For example, an initial 2.0C charging step consumes slightly more energy than a 1.0C step but results in lower overpotentials and higher efficiency during the subsequent high-rate (3.0C) step, as illustrated by the simulations (Fig. S17). Specifically, an initial charge at 2.0C consumes approximately 0.04 mWh cm^{-2} more energy compared to a 1.0C step, but this initial energy investment reduces subsequent overpotentials, recovering approximately 0.03 mWh cm^{-2} during the later charging stage. To quantify these energy differences, we assumed a fully charged battery capacity of approximately 6.8 mWh cm^{-2} (calculated as 3.4 V × 2 mAh cm^{-2}).

Notably, this trade-off between initial and subsequent charging efficiency depends on the relative electricity pricing during each charging phase. If energy prices are substantially lower during the initial charging step, a higher initial rate could be economically favorable despite higher initial energy consumption. Importantly, we observe that excessively high initial rates (e.g., above 3.0C) yield diminishing returns, as the maximum particle activation saturates, and additional energy input is lost primarily due to transport limitations rather than stored as useful boundary energy. Conversely, moderate initial rates (around 1.0–2.0C) partially store the additional invested energy within the system as boundary energy, which can be subsequently utilized to reduce later overpotentials.

For LTO electrodes, despite particle sizes similar to those of LFP, we do not observe saturation even at high currents (15.0C). This is because the active particle population—and consequently the saturation current—depends not only on particle size but also on the exchange current density. The substantially lower charge-transfer resistance of LTO compared to LFP (Fig. S22) means that fewer particles are activated even at high rates (Fig. S17), making solid-state diffusion the predominant source of overpotential. Additionally, the faster inter-particle lithium exchange in LTO significantly reduces the active particle population during the 5-hour resting period. Consequently, employing higher initial rates does not enhance efficiency during the subsequent charging steps for LTO, limiting the potential for revenue-driven optimization that was demonstrated with LFP electrodes.

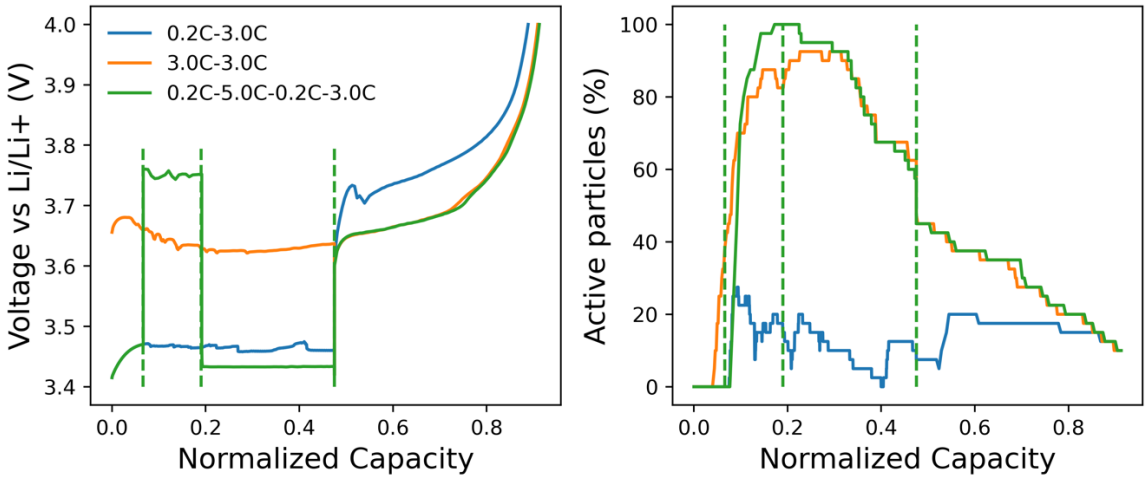

Supplementary information Fig. S18. Comparison between the previously validated memory protocols (0.2C-1h_rest-3.0C, 3.0C-1h_rest-3.0C) and a multi-step protocol (0.2C-5.0C-0.2C-1h_rest-3.0C). The dashed vertical lines correspond the changes in the multi-step protocol current.

To further demonstrate the model's capability for protocol optimization, we simulated a multi-step charging protocol consisting of:

- 0.2C charge up to 10% SOC
- 5.0C charge from 10% to 20% SOC
- 0.2C charge from 20% to 50% SOC
- 1 hour rest
- 3.0C charge up to cutoff voltage of 4.0 V.

This protocol was designed to assess whether a brief high-current pulse could activate a greater fraction of particles and influence the subsequent overpotential. As shown in Fig. S18, the active particle population rapidly increases upon application of the 5.0C pulse. Interestingly, despite the subsequent return to a low charging rate (0.2C), the phase-separated particles do not undergo lithium exchange and remain in an active state. As a result, when the 3.0C reading step is applied, the electrode follows a voltage profile similar to that of the 3.0C-3.0C protocol rather than the 0.2C-3.0C protocol. This leads to a lower overpotential during the high-rate step, demonstrating that short current pulses can effectively nucleate a large fraction of particles and enhance the electrode's kinetic response. These findings suggest that strategically incorporating brief high-rate pulses into charging protocols could serve as a tool for improving phase-separating battery materials' efficiency, particularly in fast-charging applications.

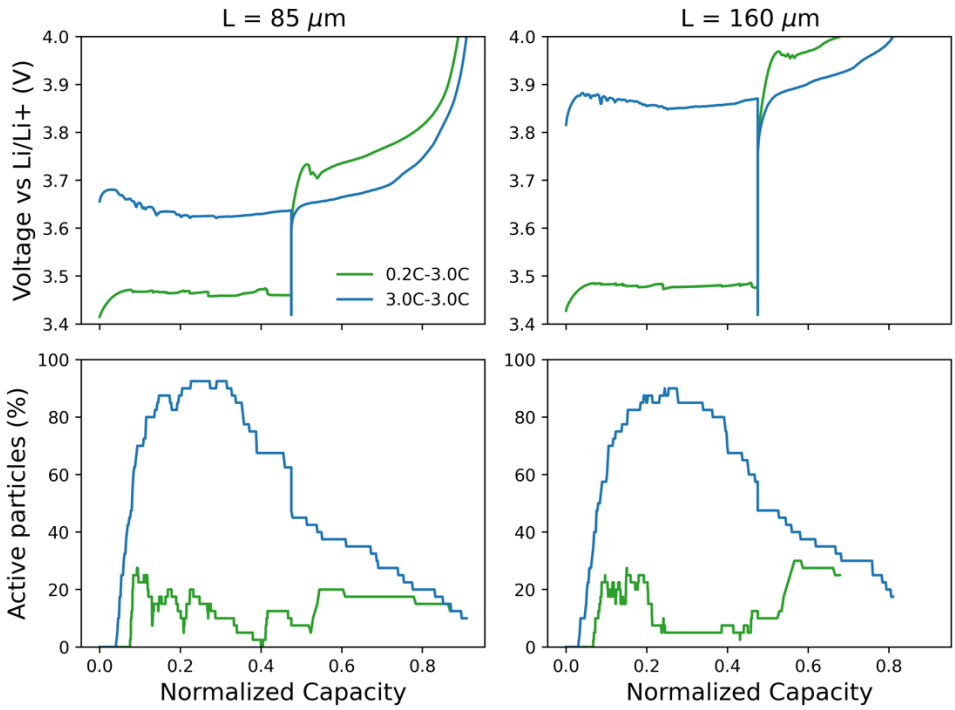

Supplementary information Fig. S19. Comparison between the LFP model results of the 0.2C-3.0C and 3.0C-3.0C protocols for the validated scenario (left) and the thicker electrode (right).

Comparing a thicker electrode (L = 160 μm) to the base case (L = 85 μm), we find that the kinetically induced memory effect remains evident. While the overall voltage increases due to the higher current density, the active particle population dynamics remain fundamentally unchanged, continuing to drive the memory effect. Additionally, we observe a slight reduction in the maximum active particle population for the 3.0C-3.0C protocol in the thicker electrode. This is attributed to greater localization of reactions toward the separator side, driven by increased electrolyte polarization within the electrode. However, this effect is relatively minor, as the dominant contributors to overpotential in this system are the diffusion and reaction limitations at the particle level.

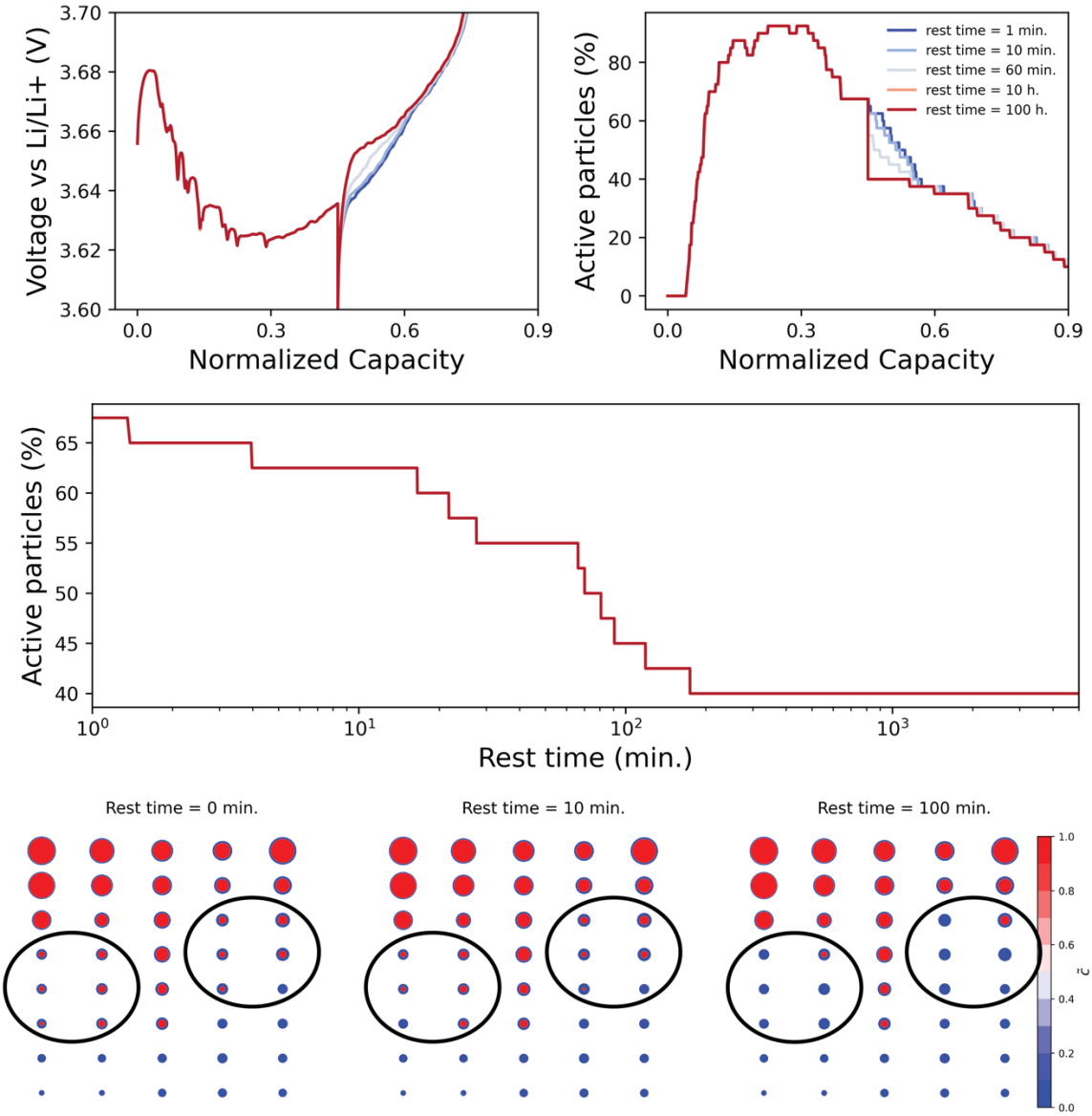

Supplementary information Fig. S20. Effect of resting time on the LFP subsequent voltage response and active particle population. Comparison between voltage profiles and active particle population at varying resting times during a 3.0C-3.0C protocol (upper figure). Active particle population evolution during resting after a 3.0C charge to 50% SOC (central figure). Solid particle concentration during resting after a 3.0C charge to 50% SOC (lower figure).

We employed the validated model to simulate the effect of a variation of the rest time. The simulations in Fig. S20 show that the voltage overpotential at the beginning of the reading step increases proportionally to the resting time. Under open-circuit conditions, inter-particle lithium exchange gradually drives the system towards a mosaic state, reducing the active particle population. This reduction follows an exponential trend, eventually saturating after approximately 200 minutes at a stable value of 40%. The reason relies on the effect of the phase boundary energy on the different

particle sizes. In smaller particles the relative energy increase due to the presence of a phase boundary is greater than in bigger particles, and consequently the drive towards a homogenous state. Combining this effect with the faster kinetics allows Li exchange between smaller particles, while the similar energies and the slower kinetics inhibit the relaxation of bigger particles.

These results further validate our interpretation that the kinetically induced memory effect is directly linked to the stability of phase-separated particles. While relaxation does occur, the relatively slow redistribution kinetics in spheroidal particles preserves the effect over experimentally relevant timescales, highlighting the importance of particle morphology in dictating the timescales of these phenomena.

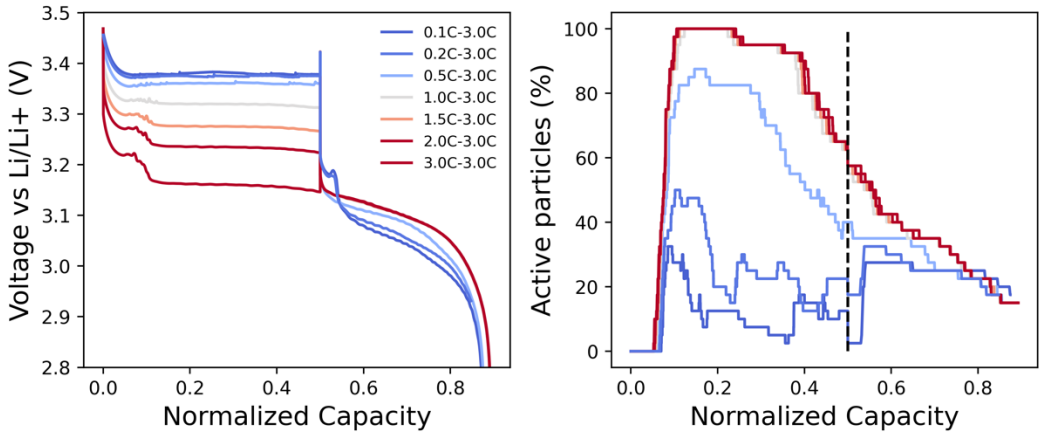

Supplementary information Fig. S21. Examples of voltage and active particle populations during discharge memory protocols for an LFP electrode.

To investigate the difference between charge and discharge on the kinetically induced memory effect, we simulated discharge memory protocols using the same model and parameters described in table T3. The results are in line with the experimental observation (Fig. S2) and allow for decupling of the LFP effect from the Graphite behaviour. Specifically, higher writing C-rates during the initial discharge step activate a larger fraction of particles, subsequently resulting in lower overpotentials during the reading step. This behaviour mirrors the previously observed charging process. However, one notable distinction arises due to differences in lithiation and delithiation kinetics, attributable to asymmetric charge-transfer behaviour (Fig. S22). As shown in literature[6], during lithiation, the autoinhibitory reaction kinetics forces the system to activate a larger particle population to sustain the same current, thus increasing the active particle fraction. Consequently, the memory effect remains observable, but the limiting current is decreased, in line with the results of Fig. S2. We can conclude that kinetic limitations originating from the Graphite electrode are responsible for the hindering of the memory effect on the voltage a full cell.

2. Supplementary methods

a. Microbeam X-ray diffraction data analysis

The raw data were analysed following the methodology outlined in the Methods section of Ref [7]. This analysis provided two datasets: the "LabeledGrainsTable" and the "EnrichedFramesTable", which store the evolution of all detected grains throughout the 0.2C–3.0C and 5.0C–3.0C memory protocols, along with the corresponding electrochemical data. The description tables legend is hereby provided.

Table T1 Legend of LabeledGrainsTable

Column name	**Description**
exp_name	ESRF experiment name.
exp_nr	ESRF experiment number.
snapshot	Internal reference.
grainnr	Number of the grain. Changing for each grain and timestep.
labelnr	Number of the labelled grain. Changing for each grain, remaining constant during time.
framenr	Number of the timestep.
point	Point of the pouch cell under the beam.
eta	Value of the grain's η at the given timestep.
omega	Value of the cell's ω at the given timestep.
twotheta	Value of the grain's 2θ at the given timestep.
deviation	Deviation from the initial 2θ value
dspace	Plane distance
hlk	Grain's reflection and phase (LFP or FP).
xmin, xmax, ymin, ymax	Values of the pixel frame for plotting.
intensity	Integral of the total intensity in the frame.
grain	2D matrix showing the intensity in the frame.

Table T2 Legend of EnrichedFramesTable

Column name	Description
Time	Date-time of the experiment
ESRFCurrent	Energy of the ring
Exposure	Data collection time in seconds
rot_angle	ω angle. Indicates z-axis rotation.
rot_angle_step	ω step angle.
sample_y	y-coordinate of the sample (indicates which location of the sample is lit)
sample_z	z-coordinate of the sample (indicates which location of the sample is lit)
FrameNr	Sequential frame number
CellNr	Number reference to the electrochemical pouch cell that was used
ExperimentNr	Number reference to the cycling experiment
CapAh	Capacity in Ah
EnWh	Energy in Wh
I	Current running through the cell
V	Voltage of the cell
Mode	Electrochemical mode: C for Charge, D for Discharge and R for Rest
ECTime	Time the current and voltage were measured. Closest available data point w.r.t. frame time

To ensure robust analysis, we selected and tracked all labelled grains that were consistently detected from the beginning to the end of the protocol and appeared in at least 35 frames. This post-processing step was necessary due to grain rotation. When a grain rotates—often as a result of contact with expanding or contracting neighbouring particles—it may fall out of the Bragg condition, preventing further detection of its reflection.

For the selected grains, we tracked their η, θ values and plotted their reflections in a 2D space across all protocol steps, as shown in Fig. 2. By analysing the number of peaks and their evolution in θ over time, we classified the grains into three categories as described in the main text, based on when they exhibit FP, LFP, or both reflections during the various protocol steps.

b. Electrochemical phase-field Model formulation.

A physics-based electrochemical model was implied to fully characterize the thermodynamic origin of the kinetically induced memory effect.

- *Particle model*

The particle behavior was modeled by considering a Cahn-Hillard phase-field formalism so that, given a normalized concentration $\tilde{c} = \frac{c}{c_{max}}$, the chemical potential of a particle with maximum concentration c_{max} is determined by the regular solution theory including the gradient energy penalty κ and the regular solution parameter Ω:

$$\mu = \mu^{\Theta} + k_B T \ln\left(\frac{\tilde{c}}{1-\tilde{c}}\right) + \Omega(1-2\tilde{c}) - \frac{\kappa}{c_{max}}\nabla^2\tilde{c}$$

where μ^{Θ} is the difference in chemical potential between the Li/Li^+ redox potential and the chemical potential of the material.

The solid concentration within the particle evolves according to linear irreversible thermodynamics:

$$\frac{dc}{dt} = \nabla \cdot \left(\frac{D}{k_B T}\nabla\mu\right)$$

where $D = D_0 c\,(1-\tilde{c})$ is the lattice diffusivity with tracer diffusivity D_0.

For the case of LFP the reaction rate R at the particle surface is calculated by using the electro-limited case of Coupled Ion Electron Transfer Theory[8,9]

$$R(c,\eta) = k_0(1-\tilde{c})\left(\frac{c_{Li^+}}{1+e^{\eta_f/k_BT}} - \frac{\tilde{c}}{1+e^{-\eta_f/k_BT}}\right)\ \mathrm{erfc}\left(\frac{\frac{\lambda}{k_BT} - \sqrt{\left(\frac{\eta_f}{k_BT}\right)^2 + 1 + \sqrt{\frac{\lambda}{k_BT}}}}{2\sqrt{\frac{\lambda}{k_BT}}}\right)$$

which consider an exchange current density k_0, electrolyte concentration c_{Li^+}, reorganization energy λ, and formal overpotential η_f, to naturally reproduce the overpotential dependence and the concentration dependence of the reaction rate for LFP[10]. The formal overpotential is defined as

$$\eta_f = \eta + \frac{k_B T}{e}\ln\left(\frac{c_{Li^+}}{c}\right)$$

where the overpotential is calculated, considering the solid phase electrical potential ϕ_s, as $\eta = \frac{\mu - \mu_{Li^+}}{e} + \phi_s$.

Finally, we clarify here some differences in the modeling for the cases of LTO and NMC811.

Given the good electrical conductivity of LTO[2] we speculate the correct approximation for the reaction rate to be the ion-couple electron transfer[8]:

$$R = k_0(1-\tilde{c})\sqrt{\tilde{c}\,c_{Li^+}}\left(e^{\frac{1}{2}\frac{e\eta}{k_BT}} - e^{-\frac{1}{2}\frac{e\eta}{k_BT}}\right)$$

Moreover, NMC811 was simulated following the more common approach to electrochemical modeling given its efficacy in the simulation of solid solution materials.

The mass conservation is considered to follow Fick's law

$$\frac{\mathrm{dc}}{\mathrm{dt}} = \nabla \cdot (\mathrm{D}(\tilde{c})\nabla \mathrm{c})$$

and the reaction rate is approximated by the Butler-Volmer equation

$$R = k_0(\tilde{c})\sqrt{c_{Li^+}}\left(e^{\frac{1}{2}\frac{e\eta}{k_B T}} - e^{-\frac{1}{2}\frac{e\eta}{k_B T}}\right)$$

Where the diffusion and the exchange current density dependence on concentration and the open circuit voltage are fitted from the work of McClelland, et al. [3,11]:

$$\mathrm{D}(\tilde{\mathrm{c}}) = \mathrm{D}_0\ 10\hat{}(-66631.56\,\tilde{\mathrm{c}}^9 + 317224.13\,\tilde{\mathrm{c}}^8 + -647127.91\,\tilde{\mathrm{c}}^7 + 740625.61\,\tilde{\mathrm{c}}^6 + -522889.49\,\tilde{\mathrm{c}}^5 + 235652.79\,\tilde{\mathrm{c}}^4 + -67638.171\,\tilde{\mathrm{c}}^3 + 11887.013\,\tilde{\mathrm{c}}^2 + -1155.894\,\tilde{\mathrm{c}} + 37.601)\ ,$$

$$\mathrm{k}_0(\tilde{\mathrm{c}}) = \mathrm{k}_0(87.15\,\tilde{\mathrm{c}}^5 - 445.05\,\tilde{\mathrm{c}}^4 + 815.43\,\tilde{\mathrm{c}}^3 - 669.95\,\tilde{\mathrm{c}}^2 + 236.09\,\tilde{\mathrm{c}} - 23.67)\ ,$$

$$\begin{aligned}\mu = -k_B T\,\big(&-0.8090\,\tilde{c} + 4.4875 - 0.0428\,\tanh\big(18.5138\,(\tilde{c} - 0.5542)\big)\\ &- 17.7326\,\tanh\big(15.7890\,(\tilde{c} - 0.3117)\big)\\ &+ 17.5842\,\tanh\big(15.9308\,(\tilde{c} - 0.3120)\big)\big)\,.\end{aligned}$$

- *Electrode-level model*

Both ionic and electronic losses along the thickness of the electrode are simulated by the commonly implied porous electrode theory. The ionic flux is considered to respect electroneutrality so that the mass and charge conservation are formalized as:

$$\varepsilon \frac{dc_{Li^+}}{dt} = \nabla \cdot (\varepsilon D_{\text{amb}} \nabla c) - \nabla \cdot \left(\frac{t^i \mathbf{i}}{e} \right) - eR_V,$$

$$0 = \nabla \cdot \mathbf{i_i} - eR_V,$$

Where R_V is the volume-average reaction rate from the reaction occurring in the volume, $\mathbf{i_i}$ is the ionic current density, ε is the porosity and e is the electron charge. Specifically, the current is calculated according to the Stefan-Maxwell model for concentrated solution theory.

The electrical conductivity along the depth of the electrode is also simulated by considering charge conservation and Ohm's law:

$$0 = -\nabla \cdot \mathbf{i_e} - eR_V$$

$$\mathbf{i_e} = -\frac{1-\varepsilon}{\tau} \sigma \nabla \varphi_s$$

$\mathbf{i_e}$ is the electrical current, τ is the tortuosity, σ is the electrical conductivity of the mixture of carbon black and LFP and φ_s is the electrical potential of the solid phase.

In addition to the standard porous electrode theory model, due to the known limited electrical conductivity of LFP particles, we considered a wiring model along the volume for the LFP simulations. In particular, the particles in the volume are randomly generated having sizes following the experimental particle size distribution. The list of particles in the specific volume is then sorted by decreasing size and considered aligned along the discrete volume. This is done to account for the better electrical connection of bigger particles. The first particle in the volume at depth x will then be in contact with the carbon black having so electrical potential $\varphi_s(x)$. The rest of the particles are wired to it, following a transmission line model, as previously adopted[6], so that, given a particle conductance G and being $\Delta\phi_{k,k+1}$ the potential difference between particle k and $k+1$ the local charge conservation requires

$$G\left(\Delta\phi_{k-1,k} - \Delta\phi_{k,k+1}\right) = -eR_k$$

for the particle k having a reaction rate R_k.

This addition, while increasing the fitting capabilities of the model, does not modify sensibly the kinetic of the system and does not influence the conclusion on the role of diffusion and reaction overpotentials in the appearance of the kinetically induced memory effect. In fact, the good carbon coating of the particles under exam guarantees high intra-particle conductivity and generates negligible overpotentials. Finally, for numerical reasons, the homogenous part of the chemical potential μ_{homog} was approximated by:

$$\mu_{homog} = k_B T \left\{ -3.405 - 15 \exp\left(-\frac{\tilde{c} - 0.02}{0.02} \right) + (1.5 - 4.3\tilde{c}) \left[\frac{1}{2} \tanh\left(\frac{\tilde{c} - 0.03}{0.05} \right) \right] \right.$$
$$\left. + 20 \left[\frac{1}{2} \tanh\left(\frac{\tilde{c} - 1}{0.06} \right) \right] \right\}$$

This closely follows the regular solution chemical potential defined above but avoids logarithmic terms which are detrimental to the numerical stability of the simulation.

The remaining set of equations is described in the work defining the software MPET[12] used for the simulations.

c. Electrochemical phase-field Model Parameters

- *Exchange Current Density* k_0

The exchange current density is of primary importance in determining the saturation current for the kinetically induced memory effect. It is therefore important to elaborate on the different functional forms assumed by the model describing its relationship with concentration and overpotential.

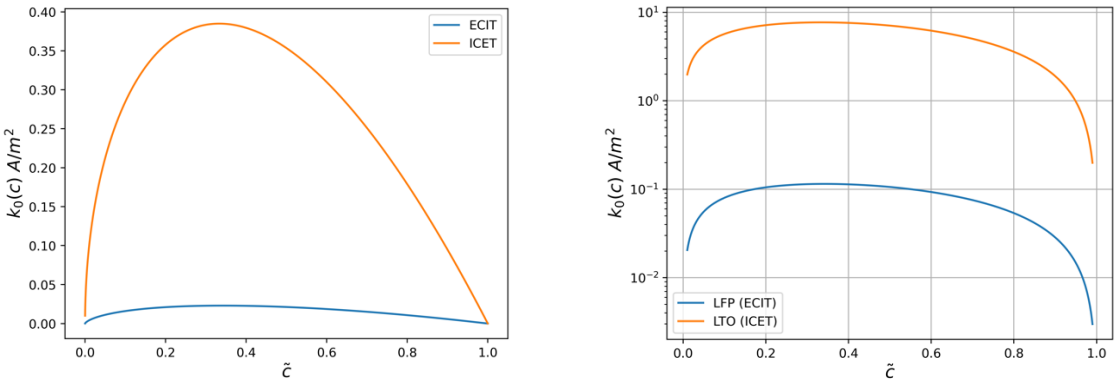

Supplementary information Fig. S22. Comparison between Electron-limited (ECIT) and Ion-limited (ICET) formalism. Comparison between ECIT and ICET for the case of $k_0 = 1$ A/m^2 (left). Comparison between the exchange current densities of LFP and LTO used in this study (right).

Given the different approximations used the real values assumed by the exchange current densities differ significantly. If the same pre-factor k_0 is used, ICET predicts a maximum exchange current density 16 times greater than ECIT. Using then the values obtained by fitting the memory protocols for LFP and LTO we can see how the real implied values differ by 2 orders of magnitude in line with the known low exchange current density of LFP[13].

- *Inter-particle conductance* G

Given the known low electrical conductivity of bulk LFP and the fundamental role of carbon coating in enhancing this feature, we approximated the inter-particle conductance as proportional to the amorphous carbon conductivity and coating thickness $G = \sigma_{carbon}\, t_{coating}$.

Considering $\sigma_{carbon} \sim 10^{-2}$ S m^{-1} and $t_{coating} = 10$ nm we obtain $G \sim 10^{-10}$ S. This value was then used as a reference value for the parameter estimation.

- *Tracer diffusivity* D_0

In LFP, the fast single-file diffusion along the [010] direction can only be properly exploited in platelet-shaped particles. On the contrary, in spheroidal commercial particles, we can expect a shirking core behavior[14] and a greater amount of defects[15] leading to an effective low tracer diffusivity.

Table T3 Parameters used for the electrochemical model of $LiFePO_4$.

Material parameters		
Enthalpy of mixing (Ω)	1.85 10^{-20} J/Li	Ref[12]
Gradient penalty (κ)	10 10^{-10} J/m	Ref[12]
Tracer diffusivity (D_0)	0.75 10^{-16} m^2/s	Best-fit
Exchange current density (k_0)	5 A/m^2	Best-fit
Reorganization Energy (λ)	3.4 10^{-20} J	Ref[13]
Electrode parameters		
Average particle radius	100 nm	Measured
Standard deviation particle radius	50 nm	Measured
Electrode thickness	85 µm	Measured
Electrode porosity	55%	Measured
Active material volume loading	85 %	Measured
Number of particles	40	
Bruggeman exponent	1.8	Best-fit
Electrical conductivity (σ)	0.4 S/m	Best-fit
Inter-particle conductance (G)	0.8 10^{-10} S	Best-fit

Table T4 Parameters used for the electrochemical model of $Li_4Ti_5O_{12}$.

Material parameters		
Enthalpy of mixing (Ω)	$1.43\ 10^{-20}$ J/Li	Ref[12]
Gradient penalty (κ)	$2.5\ 10^{-10}$ J/m	Ref[2]
Tracer diffusivity (D_0)	$4\ 10^{-16}$ m^2/s	Ref[2]
Exchange current density (k_0)	20 A/m^2	Arbitrary
Electrode parameters		
Average particle radius	100 nm	Measured[2]
Standard deviation particle radius	50 nm	Measured[2]
Electrode thickness	85 µm	Measured
Electrode porosity	30%	Measured
Active material volume loading	57 %	Measured
Number of particles	32	
Bruggeman exponent	0.5	Ref[2]
Electrical conductivity (σ)	1 S/m	Arbitrary
Inter-particle conductance (G)	1 10^{-11} S	Arbitrary

Table T5 Parameters used for the electrochemical model of $LiNi_{0.8}Mn_{0.1}Co_{0.1}O_2$.

Material parameters		
Diffusivity perfector (D_0)	10	Arbitrary
Exchange current density (k_0)	3 A/m^2	Arbitrary
Electrode parameters		
Average particle radius	10 µm	Arbitrary
Standard deviation particle radius	5 µm	Arbitrary
Electrode thickness	65 µm	Measured
Electrode porosity	30%	Measured
Active material volume loading	57 %	Measured
Number of particles	80	
Bruggeman exponent	0.5	Ref[2]
Electrical conductivity (σ)	1 S/m	Arbitrary

d. Analytical model derivation

The analytical formula presented in the main text was obtained by considering the following approximations. The electrochemical phase-field model showed the minimal impact of the long-range ionic and electronic transport on the total overpotential. This is due to the high porosity and low mass loading of the electrode under examination. We can so neglect these phenomena and assume that the electrode reacts uniformly along the thickness direction.

The geometrical parameters of the electrode can be used to compute its surface area, key parameter determining its performance. Assuming all the particles having spherical shape and radius R, we compute the total number of particles as

$$N_p = \frac{A\ t\ (1-\varepsilon)\ v}{\frac{4}{3}\ \pi\ R^3}$$

Where we considered the electrode area A, thickness t, porosity ε and volume fraction of active material v. The total surface area will so be $S = N_p\ 4\ \pi\ R^2$.

Despite the full model implying CIET theory for the reaction kinetics, that formalism does not allow a direct solution of the reaction overpotential (η_{rxn}). To avoid iterative procedures and obtain a purely analytical solution we approximate the reaction kinetics with the symmetric form of the Butler-Volmer equation:

$$i_R = S_r\ j_0\ \left(e^{\alpha\frac{e\eta_{rxn}}{k_BT}} - e^{-(1-\alpha)\frac{e\eta_{rxn}}{k_BT}}\right)$$

Where i_R is the total current at a given C-rate, S_r is the reactive surface area, j_0 is the exchange current density, and α is the charge transfer coefficient that is approximated to be 0.5 in this solution. Assuming that all the available active particles are utilized by the reading current, the reaction overpotential (η_{rxn}) can be so expressed as

$$\eta_{rxn} \cong \frac{k_BT}{e}\sinh^{-1}\left(\frac{i_R}{2\ j_0 S_r}\right)$$

The exchange current density is, generally, a function of the concentration, and thus it is evolving during the reaction process. Nevertheless, for phase-separated particles, after a relaxation process the appearing core-shell structure expose reliably a consistent (de)lithiated phase. Since our goal is to compute the initial overpotential we can consider j_0 assuming the value at the corresponding equilibrium concentration. Considering now the reactive surface area will so be proportional to total surface area S and the active particle fraction f we arrive at Eq. 1 of the main text.

The diffusion overpotential (η_{diff}) can also be computed considering a similar framework. The relaxed structure of a phase-separated particle present on the outer surface a single phase having an equilibrium concentration c_{eq}. Considering small deviation from c_{eq} the diffusion overpotential is can be approximated by knowing the surface concentration c_s as $\eta_{diff} = \frac{k_BT}{e}(\ln c_s - \ln c_{eq})$.

The relation between c_s and c_{eq} is given by a mass transfer coefficient k_m so that

$$c_s = c_{eq} + \frac{j_p}{e\, k_m}$$

where the specific current on the particle j_p relates to the total surface area and active particle fraction:

$$j_p = \frac{i_R}{S\, f}$$

Combining these equations, we reach to Eq. 2 of the main text.

The mass transfer coefficient can be related to the diffusion coefficient by approximating the flux as 1D and planar so that $k_m = D/L$ where L is the diffusion length. Assuming R as diffusion length we can relate the diffusivity and the active particle fraction with the diffusion overpotential. It must be noted that, being a phase-separating material, the effective diffusivity used in this approximation does not necessarily coincide with the tracer diffusivity used for the phase field model. However, it is safe to assume it should have the same order of magnitude.

e. Analytical model fitting procedure

The analytical approximation was to the experimental data fitted by using a differential evolution algorithm. The algorithm was chosen to assure a wide exploration of the parameter space and obtain a reliable set of parameters that could minimize the error.

The initial guess was given based on the parameters of the electrochemical phase-field model and the values of diffusivity (D) and exchange current density (j_0) were bounded to be within the same order of magnitude as the electrochemical parameters.

f. Analytical model parameters

Table T6 Parameters used for the overpotential approximation of $LiFePO_4$.

Effective Diffusivity (D)	$0.16\ 10^{-16}\ \mathrm{m^2/s}$	Best-fit
Exchange current density (j_0)	$0.594\ 10^{-3}\ \mathrm{A/m^2}$	Best-fit
Maximum active particle fraction (f_{max})	0.424	From phase-field
w	2.24	Best-fit
b	0.844	Best-fit
Particle radius (R)	200 nm	From phase-field
Electrode thickness (t)	85 µm	Measured
Electrode porosity (ε)	55%	Measured
Active material volume loading (v)	85 %	Measured

Table T7 Parameters used for the overpotential approximation of $Li_4Ti_5O_{12}$.

Effective Diffusivity (D)	$0.647\ 10^{-17}\ \mathrm{m^2/s}$	Best-fit
Exchange current density (j_0)	$1\ \mathrm{A/m^2}$	Best-fit
Maximum active particle fraction (f_{max})	0.796	Best-fit
w	0.26	Best-fit
b	8.98	Best-fit
Particle radius (R)	200 nm	From phase-field
Electrode thickness (t)	85 µm	Measured
Electrode porosity (ε)	30%	Measured
Active material volume loading (v)	57 %	Measured

Supplementary References

1. Ombrini, P., Bazant, M. Z., Wagemaker, M. & Vasileiadis, A. Thermodynamics of multi-sublattice battery active materials: from an extended regular solution theory to a phase-field model of LiMnyFe1-yPO4. *npj Comput Mater* **9**, 148 (2023).
2. Vasileiadis, A. *et al.* Toward Optimal Performance and In-Depth Understanding of Spinel $Li_4Ti_5O_{12}$ Electrodes through Phase Field Modeling. *Adv. Funct. Mater.* **28**, 1705992 (2018).
3. Karanth, P. *et al.* A phase inversion strategy for low-tortuosity and ultrahigh-mass-loading nickel-rich layered oxide electrodes. *Cell Reports Physical Science* 101972 (2024) doi:10.1016/j.xcrp.2024.101972.
4. Zhuang, D. & Bazant, M. Z. Scaling analysis of mosaic phase separation in Li-ion batteries. *Phys. Rev. E* **110**, 064142 (2024).
5. Galuppini, G. *et al.* Nonlinear identifiability analysis of Multiphase Porous Electrode Theory-based battery models: A Lithium Iron Phosphate case study. *Journal of Power Sources* **573**, 233009 (2023).
6. Li, Y. *et al.* Current-induced transition from particle-by-particle to concurrent intercalation in phase-separating battery electrodes. *Nature Mater* **13**, 1149–1156 (2014).
7. van Hulzen, M., Ooms, F. G. B., Wright, J. P. & Wagemaker, M. Revealing Operando Transformation Dynamics in Individual Li-ion Electrode Crystallites Using X-Ray Microbeam Diffraction. *Front. Energy Res.* **6**, 59 (2018).
8. Bazant, M. Z. Unified quantum theory of electrochemical kinetics by coupled ion-electron transfer. *Faraday Discuss.* 10.1039.D3FD00108C (2023) doi:10.1039/D3FD00108C.
9. Fraggedakis, D. *et al.* Theory of coupled ion-electron transfer kinetics. *Electrochimica Acta* **367**, 137432 (2021).

10. Zhao, H. *et al.* Learning heterogeneous reaction kinetics from X-ray videos pixel by pixel. *Nature* **621**, 289–294 (2023).

11. McClelland, I. *et al.* Direct Observation of Dynamic Lithium Diffusion Behavior in Nickel-Rich, $LiNi_{0.8}Mn_{0.1}Co_{0.1}O_2$ (NMC811) Cathodes Using *Operando* Muon Spectroscopy. *Chem. Mater.* **35**, 4149–4158 (2023).

12. Smith, R. B. & Bazant, M. Z. Multiphase Porous Electrode Theory. *J. Electrochem. Soc.* **164**, E3291–E3310 (2017).

13. Bai, P. & Bazant, M. Z. Charge transfer kinetics at the solid–solid interface in porous electrodes. *Nat Commun* **5**, 3585 (2014).

14. Fraggedakis, D. *et al.* A scaling law to determine phase morphologies during ion intercalation. *Energy Environ. Sci.* **13**, 2142–2152 (2020).

15. Malik, R., Burch, D., Bazant, M. & Ceder, G. Particle Size Dependence of the Ionic Diffusivity. *Nano Lett.* **10**, 4123–4127 (2010).